

Study of structural and electrical properties of Cd²⁺ doped Mn-Zn ferrites synthesized by co-precipitation method

Z. H. Nawaz^a, Khalid M. Elhindi^b, M. I. Arshad^a, S. Mumtaz^c, N. Amin^{a*}

^a Department of Physics, Government College University, Faisalabad, Pakistan 38000

^b Plant Production Department, College of Food & Agriculture Sciences, King Saud University, P.O. Box 2460, Riyadh 11451, Saudi Arabia

^c Electrical and Biological Physics, Kwangwoon University, Seoul 01897, South Korea

The main purpose of this work was to study the electrical, structural and optical properties of Cd-doped Zn based soft ferrites. A series of nano-particles with composition $Zn_{0.5}Mn_{0.5-x}Cd_xFe_2O_4$ ($x= 0.00, 0.01, 0.03, 0.05, 0.07, 0.09$) prepared by the Co-precipitation route. After preparing, the samples sintered at temperature 900°C for 6 hours. Different characterization techniques like XRD (X-Ray-Diffraction), FTIR (Fourier-Transform-Infrared-spectroscopy), UV-vis. and IV-characteristics were used to explore the effect of doping element (Cd) on the electrical, structural and optical properties of Nano-particles. XRD data confirmed the single phase of material with second phase of Fe₂O₃ and average crystalline size in range from 38.09-45.15 nm. The value of average lattice constant for the prepared material found in range from 8.4471 Å to 8.4763 Å. In FTIR data one prominent band is found in all sample and in some sample second band was found in range from 400-4000cm⁻¹. IV-observation revealed the dependence of DC-resistivity on temperature and the value for activation energy (ΔE) found in range from 0.1365 to 0.4332 eV/1000K. The UV-vis. analysis confirm the absorption peak for all samples at average wavelength 286 nm. At this wavelength absorption for all samples was in range from 2.8722-3.2956 (a.u). Cd concentration is responsible for the decrease of saturation magnetizations and losses. Due to suitable properties, these materials are useful in different fields like Recording-Media, high-frequency applications and many branches of electronic engineering etc.

(Received October 16, 2024; Accepted December 11, 2024)

Keywords: Nano structure, Co-Precipitation method, XRD, Crystalline size, Resistivity, Activation energy

1. Introduction

Spinel ferrites are a class of magnetic materials with the general formula AB₂O₄, where A and B represent different metal cations and O is oxygen. They have a cubic crystal structure known as the spinel structure, named after the mineral spinel. Spinel ferrites exhibit a combination of magnetic, electrical, and structural properties that make them useful in a wide range of applications, including magnetic storage, transformers, inductors, and biomedical devices [1].

The spinel structure can be viewed as a cubic close-packed arrangement of oxygen ions, with metal cations occupying two types of interstitial sites: tetrahedral sites (A-sites), coordinated by four oxygen atoms, and octahedral sites (B-sites), coordinated by six oxygen atoms. In spinel ferrites, the cations A and B are typically divalent (e.g., Fe²⁺, Mn²⁺, Zn²⁺ and trivalent (e.g., Fe³⁺, Al³⁺, Cr³⁺ metal ions. For instance, in the common ferrite Fe₃O₄ (magnetite), A-sites are occupied by Fe³⁺, and B-sites are occupied by a mix of Fe²⁺ and Fe³⁺ ions. Spinel ferrites are categorized into normal spinel structures, where A-sites have divalent cations and B-sites have trivalent cations, and inverse spinel structures, where A-sites hold trivalent cations while B-sites contain both divalent and trivalent cations [2].

* Corresponding author: nasir786a@yahoo.com

<https://doi.org/10.15251/JOR.2024.206.867>

Spinel ferrites are ferromagnetic, meaning they exhibit spontaneous magnetization due to the alignment of magnetic moments of ions in opposite directions. In ferrites, the magnetic moments of ions on the tetrahedral and octahedral sites align anti-parallel, but due to unequal magnetic moments, a net magnetic moment exists. The magnetism is primarily attributed to iron ions (Fe^{3+}) with unpaired electrons. Substituting other divalent cations such as Mn^{2+} , Ni^{2+} , Zn^{2+} , Co^{2+} in the lattice can modify magnetic behavior. Key magnetic properties include high Curie temperature, low coercivity (resistance to demagnetization), and high permeability, which make them ideal for soft ferrites used in transformers and inductors [3-5].

Spinel ferrites are semiconductors, meaning they have relatively low electrical conductivity compared to metals. Conductivity in ferrites is mainly due to the hopping of electrons between ions of the same element in different oxidation states, such as Fe^{2+} and Fe^{3+} . This hopping is thermally activated, leading to an increase in conductivity with temperature. Their high electrical resistivity makes them ideal for applications where minimizing eddy current losses is important, such as in transformer cores and electromagnetic interference suppression [6-8].

Spinel ferrites find diverse applications. In magnetic storage devices, ferrites like NiFe_2O_4 and CoFe_2O_4 are used in magnetic tapes, recording heads, and permanent magnets. Soft ferrites, such as MnFe_2O_4 , with low coercivity and high permeability, are used in transformers and inductors. Biomedical applications leverage superparamagnetic nanoparticles of ferrites (e.g., Fe_3O_4) for drug delivery, MRI contrast agents, and hyperthermia treatments for cancer. Additionally, spinel ferrites are useful in catalysis due to their surface properties and active sites for chemical reactions [9].

Spinel ferrites can be synthesized through various methods, each influencing the particle size, morphology, and properties of the material. The solid-state reaction method involves heating a mixture of oxides or carbonates of metals to form ferrites at high temperatures. In the chemical co-precipitation method, metal salts are precipitated together to form a precursor, followed by thermal treatment. The sol-gel method forms gel-like materials from metal alkoxides or salts, which are heated to form ferrites. Hydrothermal synthesis involves using high-pressure and temperature conditions to crystallize ferrite particles from aqueous solutions. Each synthesis method allows control over particle size and shape, affecting the ferrite's magnetic and electrical properties [10, 11].

Spinel ferrites offer a versatile platform for developing materials with tailored magnetic and electrical properties, making them essential in both traditional and advanced technological applications. According to the best of my knowledge a very less work is done in which the cadmium is doped in Manganese-Zinc ferrites. The cadmium in manganese-zinc ferrites and studied the effect of Cd^{2+} ions on structural and electrical properties of the prepared material having composition $\text{Zn}_{0.5}\text{Mn}_{0.5-x}\text{Cd}_x\text{Fe}_2\text{O}_4$ ($x = 0.00, 0.01, 0.03, 0.05, 0.07, 0.09$).

2. Materials and methods

A series of soft ferrites having chemical formula $\text{Zn}_{0.5}\text{Mn}_{0.5-x}\text{Cd}_x\text{Fe}_2\text{O}_4$ ($x = 0.00, 0.01, 0.03, 0.05, 0.07, 0.09$) prepared by the chemical route called as co-precipitate route. The materials used in process are $\text{CdCl}_2 \cdot 2\text{H}_2\text{O}$, $\text{MnCl}_2 \cdot 4\text{H}_2\text{O}$, ZnCl_2 , FeCl_3 and NaOH .

There are several methods by which we can prepare the ferrites such as hydrothermal process, Sol-Gel method, Auto-Combustion route and Co-precipitate method [19-24]. The co-precipitate method has some advantages over other methods due to which we used co-precipitate method to prepare the sample.

First, the chemicals weighted according to their mole ratio and dissolved the chemicals into beaker and stirred for 30 minutes. During the stirring process the solution of Sodium-Hydroxide added into the beaker to keep the pH about 12. During the stirring process the precipitates of the solution were seen. After stirring process, the solution which had precipitates located into the water bath for two hours at temperature about 80°C . Then the solution of precipitate filtered by filter paper and washed by De-ionized water, ethanol and methanol to reduce the impurity. After filtration process the prepared precipitates dried in oven for overnight at temperature 80°C . When the prepared sample dried completely then the sample grinded for half hour to get fine powder of sample and then placed the sample in furnace for six hours at 900°C to sinter the sample. After sintering the

sample, the sample again grinded for half hour in mortar and pestle to make fine powder. Finally, the sample prepared and ready for characterization. The mention process in above discussion explained by flow chart of co-precipitation method.

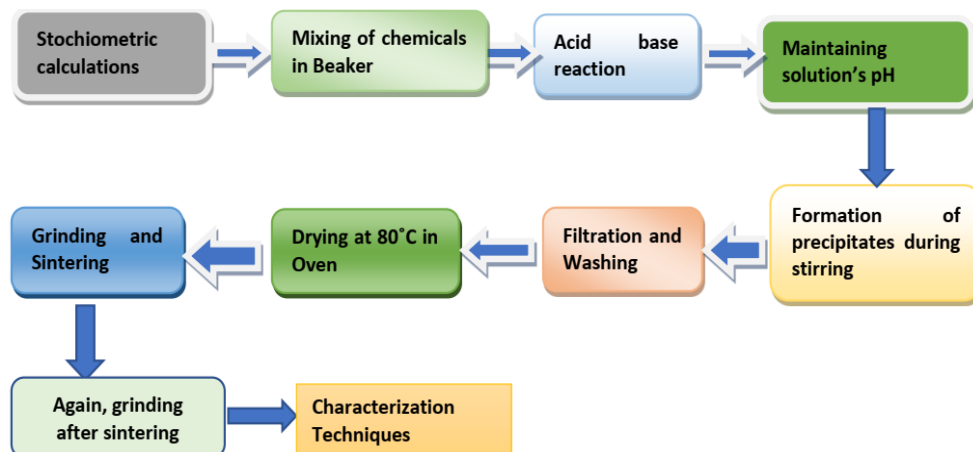


Fig. 1. Step by step preparation method.

The prepared sample having chemical composition $Zn_{0.5}Mn_{0.5-x}Cd_xFe_2O_4$ ($x = 0.00, 0.01, 0.03, 0.05, 0.07, 0.09$) prepared by the soft-chemical route called co-precipitation route characterized by different characterization techniques. We characterized the sample by four techniques in which XRD (X-Ray-Diffraction), IV-Characteristics, FT-IR (Fourier-Transform-Infrared-Spectroscopy and UV-Visible. The details of results which we got by these characterization techniques are explained as follows.

3. Result and discussion

3.1. X-ray diffraction analysis

In this portion, we explained the structural information of the prepared sample. The sample of cadmium doped zinc-manganese-ferrite characterized by the XRD (X-ray-diffraction) and calculated different parameters like interplanar-distance (d), Full-Width-Half-Maxima (β), Lattice-Constant (a), volume (V), size of crystalline (D) and the density of x-ray (ρ). We used following expressions to calculate the required parameters. By using plane-spacing relation,

$$a = d\sqrt{h^2 + k^2 + l^2} \quad (1)$$

According to Bragg's-law,

$$2d\sin\theta = n\lambda \quad (2)$$

Comparing equation (1) and (2) we can write as,

$$a = \frac{\lambda}{2\sin\theta} \sqrt{h^2 + k^2 + l^2} \quad (3)$$

The unit-cell volume is given by,

$$V_{\text{cell}} = a^3 \quad (4)$$

The crystalline-size can be calculated with help of Scherrer-formula,

$$D = \frac{k\lambda}{\beta_{(hkl)}\cos\theta_B} \quad (5)$$

where 'k' is shape-factor having value 0.89-0.90, ' λ ' denote wavelength of x-rays, ' β ' denote the value of full-width-half-maxima and D be the size of crystalline.

And the density of x-rays can be obtained by following relation,

$$\rho_{X\text{-ray}} = \frac{8M}{N_A V} \quad (6)$$

where 'V' be the unit-cell volume, 'M' be the molecular-weight of the sample and 'NA' be the Avogadro's-number (6.0221×10^{23} per mol). The figure shows the X-Ray-Diffraction of $Zn_{0.5}Mn_{0.5-x}Cd_xFe_2O_4$. From XRD results we seen that sample exhibit simple cubic structure having major phase the second phase was also observed which is of Fe_2O_3 . The secondary phase of Fe_2O_3 was obtained at the boundaries due to the high reactivity between the ferric and cadmium ions. The prepared ferrites are spinel ferrites. The spinel structure of the prepared sample was confirmed by the peaks which comparable to planes (220), (311), (400) and (333/511). It had been found different parameters like lattice-constant, crystalline-size and density of x-rays with help of XRD data. It had been observed the value of lattice constant found in range from 8.4471 Å to 8.4763 Å. The value for crystalline size observed in range from 45.15 nm to 38.09 nm. The value for density of x-rays found in range from 5.1572 g/cm³ to 5.2846 g/cm³. A minor variation in the lattice parameters of spinel ferrites occur due to several factors, with cation substitution being a key reason. When metal cations of different ionic radii replace each other in the tetrahedral (A-site) or octahedral (B-site) positions, the lattice expands or contracts to accommodate the size difference [12, 13].

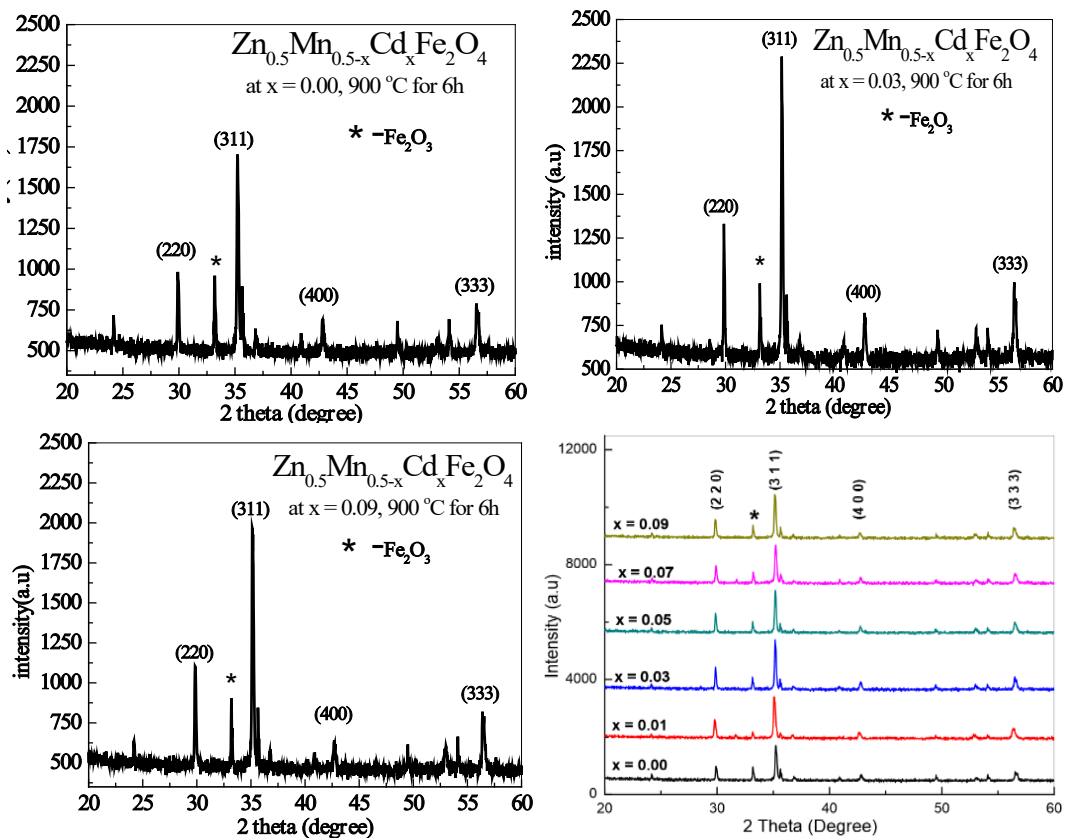


Fig. 2. XRD pattern of $Zn_{0.5}Mn_{0.5-x}Cd_xFe_2O_4$ ($x = 0.00, 0.01, 0.03, 0.05, 0.07, 0.09$).

Cation distribution also plays a role, as spinels can exhibit normal or inverse structures, where the rearrangement of cations between sites affects the unit cell dimensions [14]. Temperature influences lattice parameters through thermal expansion, with the lattice expanding as temperature rises, especially around the Curie temperature. External pressure compresses the lattice, reducing interatomic distances, while oxygen vacancies introduce local distortions that alter the lattice. Strain effects in thin films or nanoparticles due to surface tension or lattice mismatch can further modify the lattice structure, leading to variations compared to bulk materials. All these factors contribute to the overall change in the lattice parameters of spinel ferrites [15, 16].

3.2. UV–visible spectroscopy

In this section, we discussed the optical properties of the prepared samples of chemical formula $Zn(0.5)Mn(0.5-x)Cd(x)Fe_2O_4$ ($x = 0.00, 0.01, 0.03, 0.05, 0.07, 0.09$). It had been observed the prominent band for absorption in ultraviolet region at wavelength 286 nm. The absorption bands are shown in figure 2.

The values for absorption found in all samples placed in table 1 corresponding to their concentration. It is seen that the absorption lies in range from 2.8722 to 3.2956.

Table 2. Absorption of samples for $x = 0.00, 0.01, 0.03, 0.05, 0.07, 0.09$.

Concentration	0.00	0.01	0.03	0.05	0.07	0.09
Absorption	2.9089	3.2584	3.2956	2.9331	2.8722	3.1847
Frequency (nm)	286.3810	286.4903	286.2644	286.2544	286.4950	286.4903

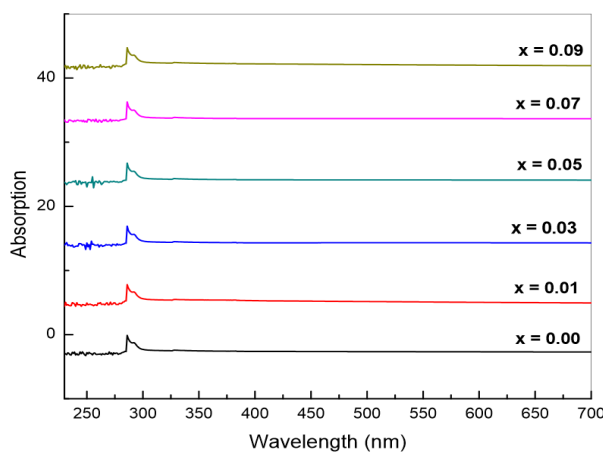


Fig. 3. UV-vis. absorption spectrum of $Zn(0.5)Mn(0.5-x)Cd(x)Fe_2O_4$ ($x = 0.00, 0.01, 0.03, 0.05, 0.07, 0.09$).

3.3. FTIR analysis

The FTIR (Fourier-Transform-Infrared-Spectroscopy) observation done in range from 450 cm^{-1} to 4000 cm^{-1} and range of transmittance percentage was in range from 70 to 100 as shown in figure 3. One prominent band is observed at wavenumber range from 539.14 cm^{-1} to 540.35 cm^{-1} in all samples by which we confirmed the band-formation at octahedral-sites between metal-ions and oxygen-ions. The second band was observed in between of 1100 cm^{-1} to 1600 cm^{-1} . in some samples which confirmed the presence of tetrahedral-sites. The formation of these bands is due to the vibration of atoms at octahedral and tetrahedral sites.

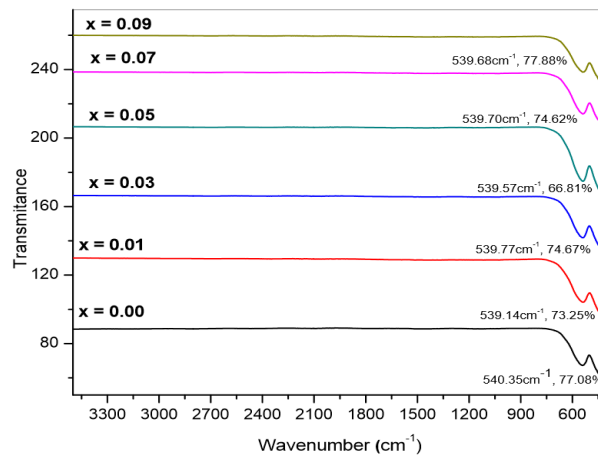


Fig. 4. FTIR spectrum of $Zn_{(0.5)}Mn_{(0.5-x)}Cd_{(x)}Fe_2O_4$ ($x = 0.00, 0.01, 0.03, 0.05, 0.07, 0.09$).

3.4. Raman spectroscopy

Raman spectroscopy is a valuable technique for analyzing spinel ferrites, offering insights into their vibrational properties, cation distribution, and structural integrity [17]. Spinel ferrites have a cubic structure with the space group $Fd\bar{3}m$, which gives rise to five characteristic Raman-active modes: A_{1g} , E_g and three T_{2g} modes [18, 19]. These modes correspond to various vibrational motions, such as the symmetric stretching of metal-oxygen bonds (primarily tetrahedral cations for A_{1g} and asymmetric bending or stretching of bonds in octahedral and tetrahedral sites for T_{2g}). Shifts in these vibrational peaks can reveal critical information about cation distribution in the structure [20]. For instance, cation substitution (e.g., Zn^{2+} , Ni^{2+}) alters bond lengths and angles, leading to changes in Raman peak positions, especially for A_{1g} and T_{2g} modes. Raman spectra can also detect lattice distortions or defects like oxygen vacancies, which affect bond lengths and contribute to peak broadening or shifting. This makes Raman spectroscopy a key method for identifying non-stoichiometry and structural defects in ferrites. Additionally, in nanostructured spinel ferrites, size-dependent effects become evident in the Raman spectra, with nanoparticle samples often showing broadened peaks due to surface disorder and strain. Such variations in Raman signatures can provide insights into the crystallinity and particle size of spinel ferrites, making it a crucial tool for understanding their structural, magnetic, and electrical behavior.

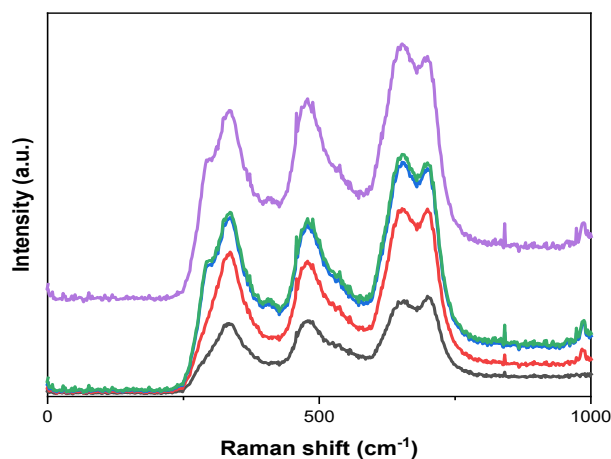


Fig. 5. Raman spectrum of $Zn_{(0.5)}Mn_{(0.5-x)}Cd_{(x)}Fe_2O_4$ ($x = 0.00, 0.01, 0.03, 0.05, 0.07, 0.09$).

3.5. Current voltage analysis

In this section, we described the electrical properties of the prepared sample. The prepared samples were examined by the Keithley-Electrometer 2401 model and collected results at different temperatures. In this type of characterization first we prepared the pellets of the materials under discussion with help of hydraulic press and kept the pressure about 15 ton for time about half an hour. After making pellets the prepared pellets were placed to found the electrical properties of samples. Each sample was examined at different values of temperatures like 250 °C, 300 °C, 350 °C, 400 °C, 450 °C, 500 °C, 550 °C and 600 °C. The value of DC-resistivity was calculated by using the relation of equation 7.

$$\rho = \frac{RA}{d} \quad (7)$$

In the above equation, the “A” denotes the area of pellet, “d” denotes the pellet’s thickness, “R” is the resistance of sample and ρ denotes the resistivity of sample. First, we found the resistance of sample with help of IV-Graph because slope of IV-Graph is equal to inverse of resistance of sample.

$$\text{Slope} = \frac{\Delta I}{\Delta V} \quad (8)$$

And according to Ohm’s law,

$$R = \frac{\Delta V}{\Delta I} \quad (9)$$

On comparison equation 8 and 9,

$$R = 1/\text{Slope} \quad (10)$$

The values of resistance of every sample at all temperatures were calculated with help of relation 10 and then using expression 7 the resistivity of sample at all temperatures were calculated. The graph between temperature and resistivity as shown in figure 6.

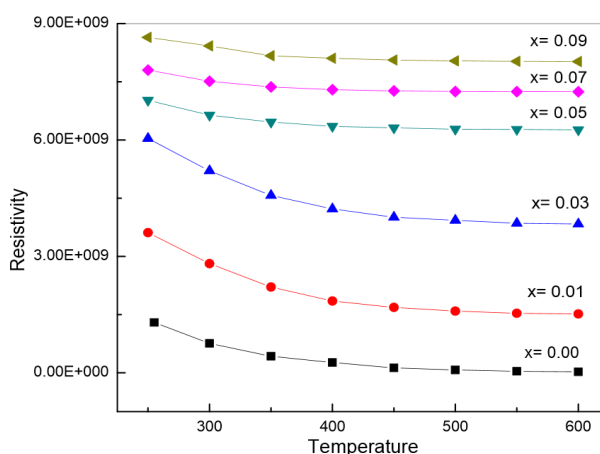


Fig. 6. Relation between the temperature and resistivity.

It was described from the relation between temperature and resistivity that the resistivity of all samples decreased by increasing the temperature. When the temperature increased the resistivity decreased.

In order to calculate the activation energy for each sample, we described the relation between the resistivity and the temperature. T Arrhenius-equation described the relation between temperature and the resistivity as given in equation 4.11,

$$\rho = \rho_0 e^{-\Delta E/KT} \tag{11}$$

In the above expression ΔE represents the activation-energy of the material and ‘T’ is the absolute temperature and K represents the Boltzmann-Constant. It is clear from the figure that the DC-resistivity varies with temperature. By solving equation 11 we can find the expression for the activation energy of material.

After taking natural log of equation 11, the equation becomes,

$$\ln \rho = - \Delta E/k(1/T) + \ln \rho_0 \tag{12}$$

As we know that,

$$y = mx + c \tag{13}$$

comparing equation 12 and 13,

$$m = \Delta E/k, \qquad \Delta E = mk \tag{14}$$

where m is the slope and k is the Boltzmann-constant. If we have values of Boltzmann-Constant and slope then we can find out the activation energy of material. The slope in equation 14 found with help of graph between $\ln\rho$ and $1000/T$ as shown in figure 7.

Table 2. Activation energy of Cd doped Zn Mn ferrites for x = 0.00, 0.01, 0.03, 0.05, 0.07, 0.09.

Value of x	0.00	0.01	0.03	0.05	0.07	0.09
Activation Energy (eV/1000K)	0.1458	0.1527	0.1365	0.1553	0.4332	0.1880

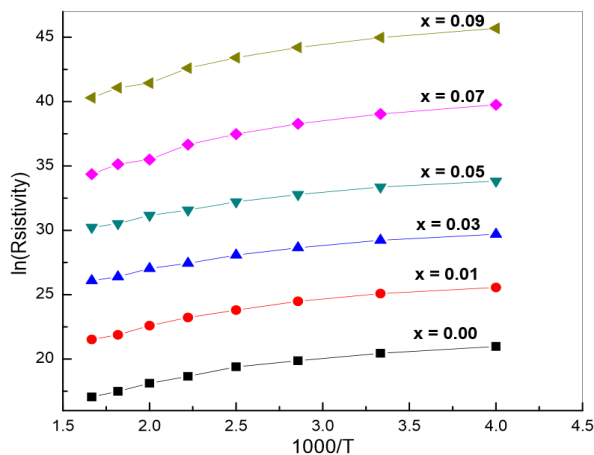


Fig. 7. Variation of Ln (Resistivity) with 1000/T for x = 0.00, 0.01, 0.03, 0.05, 0.07, 0.09.

With help of the above graph we calculated the slope and then by using equation (14) we calculated the activation energy for each sample. Which is found in range of 0.1365 eV/1000K to 0.1880 eV/1000K. The value of activation energy for all samples given below in table 2.

3.6. Dielectric analysis

The figure 8 illustrates the conductance vs. frequency behavior for spinel ferrites with different substitution levels (x). At low frequencies, conductance remains nearly constant across all samples, indicating that DC conductivity dominates, with minimal impact from substitution. This suggests that charge carrier hopping between Fe^{2+} and Fe^{3+} ions can keep pace with the low-frequency AC field. As the frequency increases, conductance rises, reflecting the frequency-dependent nature of charge carrier hopping. The undoped sample ($x = 0.0$) exhibits a more pronounced increase in conductance compared to the substituted samples, suggesting that substitution impedes carrier mobility. At higher frequencies, the conductance diverges, with the undoped sample showing the highest values, while the substituted samples, particularly those with higher x , demonstrate reduced conductance. This reduction can be attributed to structural distortions, alterations in the Fe-O-Fe bond angles, or increased grain boundary scattering introduced by substitution, which limits the hopping conduction. Additionally, the lower conductance in substituted samples at high frequencies may be due to the Maxwell-Wagner polarization effect, where charge carriers accumulate at interfaces or grain boundaries. As x increases, this polarization and interfacial charge accumulation are less pronounced, reducing the overall conductance. Thus, substitution in spinel ferrites effectively suppresses high-frequency conductance while having a smaller effect at lower frequencies.

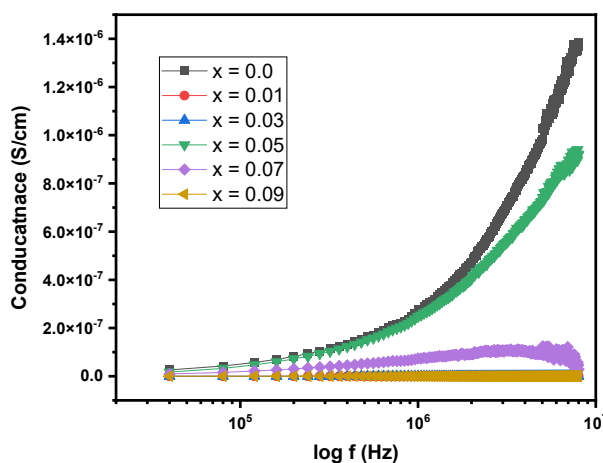


Fig. 8. Conductance with frequency for $x = 0.00, 0.01, 0.03, 0.05, 0.07, 0.09$.

3.7. Magnetic analysis

The as-prepared samples have soft magnetic nature. The addition of Cd reduced all parameters of magnetizations determined by the hysteresis loops. The decrease in coercivity indicates that losses are small with soft magnetization. The saturation magnetization (M_s) exhibits a variable trend with increasing Cd^{2+} concentration. This variability is attributed to the presence of anomalous factors and secondary phases [21]. Similarly, coercivity (H_c) also shows variability with increasing Cd^{2+} ions, as detailed in Table 3. The maximum values of saturation magnetization and remanence magnetization are observed at $x = 0.00$, with values of 37.83 emu/g and 30.96 emu/g, respectively. As the Cd is nonmagnetic addition of Cd reduced the saturation magnetizations, and the minimum value is observed for $x=0.09$. The magnetic properties of soft ferrites are influenced by factors such as grain size, synthesis technique, and cation distribution [21]. As the losses are small these materials may be used for the magnetic applications operational by low energy losses [22].

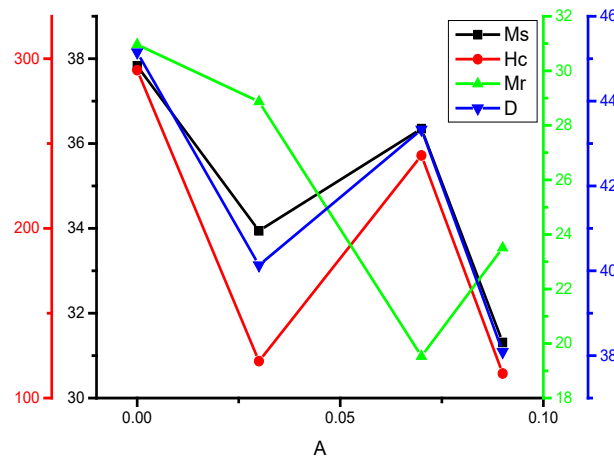


Fig. 9. Magnetic parameters vs Cd concentrations in ZnMn ferrites.

The table 3 presents the magnetic parameters including saturation magnetization (M_s), coercivity (H_c), and remanence (M_r) of as-prepared ferrites with varying substitution levels (x). For $x = 0.00$ (no substitution), M_s is 37.83 emu/g, H_c is 293.25 Oe, and M_r is 30.96 emu/g, indicating strong magnetization and high coercivity. As substitution increases to $x = 0.03$, M_s decreases to 33.94 emu/g and H_c drops significantly to 121.72 Oe, suggesting a reduction in the overall magnetic strength and easier magnetization reversal. For $x=0.07$, M_s rises slightly to 36.35 emu/g, and H_c increases to 242.96 Oe, reflecting an intermediate behavior with improved saturation magnetization but still lower than the undoped sample. At $x=0.09$, both M_s and H_c reach their lowest values of 31.31 emu/g and 114.45 Oe, respectively, indicating a significant decrease in magnetic strength and coercivity. The remanence (M_r) shows a similar trend, decreasing overall with substitution, with the lowest value at $x = 0.07$. This behavior suggests that cation substitution in ferrites disrupts the magnetic structure, reducing the magnetization and making magnetization reversal easier, especially at higher x values [23].

Table 3. Magnetic parameters of LMMC ferrites.

x	M_s	H_c	M_r
0.00	37.83	293.25	30.96
0.03	33.94	121.72	28.87
0.07	36.35	242.96	19.53
0.09	31.31	114.45	23.51

4. Conclusion

The Cd doped Zn-Mn ferrites were prepared with co-precipitation method. The prepared ferrites exhibited the structure of spinel ferrites. The prepared sample had not single-phase sample but was secondary phase which was of Cd_2O_3 . It had been confirmed the formation of spinel-phase. The lattice constant found in range from 8.4471 Å to 8.4763 Å and crystalline size found in range 38.09 nm to 45.15 nm. The x-rays density value found in range from 5.1572 g/cm³ to 5.2846 g/cm³. The FT-IR data revealed the vibration of atoms at octahedral and tetrahedral sites. In FTIR data one band is found in all sample and in some sample two bands were found in range from 400-4000cm⁻¹. IV-observation revealed the dependence of DC-resistivity on temperature and the value for activation energy (ΔE) found in range from 0.1365 to 0.4332 eV/1000K. The UV-vis. analysis confirm the absorption peak for all samples in ultraviolet region at average wavelength 286 nm. At this wavelength absorption for all samples was in range from 2.8722-3.2956. Due to the properties mentioned above these materials are useful in field of Telecommunication, industry and electronic-field.

Funding

Researchers Supporting Project number (RSPD2024R952), King Saud University

Acknowledgements

The authors extend their deep appreciation to Researchers Supporting Project number (RSPD2024R952), King Saud University, Riyadh, Saudi Arabia.

References

- [1] L. Khudaysh, I.A. Ahmed, S.R. Ejaz, S.A. Khan, Y.A. Haleem, M.M. Ibrahim, M. Ali, H.M.T. Farid, Z.M. El-Bahy, *Journal of Rare Earths*, 42 (2024) 1755-1763; <https://doi.org/10.1016/j.jre.2023.10.013>
- [2] R. Khan, Zulfiqar, S. Fashu, M.-U. Rahman, *Journal of Materials Science: Materials in Electronics*, 27 (2016) 7725-7730; <https://doi.org/10.1007/s10854-016-4759-z>
- [3] C. Kolekar, P. Kamble, A.J.J.o.m. Vaingankar, *Materials*, 138 (1994) 211-215; [https://doi.org/10.1016/0304-8853\(94\)90418-9](https://doi.org/10.1016/0304-8853(94)90418-9)
- [4] A.U. Rehman, N. Morley, N. Amin, M.I. Arshad, M.A. un Nabi, K. Mahmood, A. Ali, A. Aslam, A. Bibi, M.Z. Iqbal, *Ceramics International*, 46 (2020) 29297-29308; <https://doi.org/10.1016/j.ceramint.2020.08.106>
- [5] A.U. Rehman, S. Sharif, H. Hegazy, N. Morley, N. Amin, M. Akhtar, M.I. Arshad, Z. Farooq, Z. Munir, T. Munir, *Materials Today Communications*, (2023) 105371; <https://doi.org/10.1016/j.mtcomm.2023.105371>
- [6] M.J. Sadiq Mohamed, S. Caliskan, M.A. Gondal, M.A. Almessiere, A. Baykal, Y. Slimani, K.A. Elsayed, M. Hassan, I.A. Auwal, A.Z. Khan, *ACS Applied Nano Materials*, 6 (2023) 7330-7341; <https://doi.org/10.1021/acsanm.3c00464>
- [7] A.U. Rehman, G. Abbas, B. Ayoub, N. Amin, M.A. un Nabi, N.A. Morley, M. Akhtar, M.I. Arshad, M.U. Khalid, M. Afzaal, *Materials Science and Engineering: B*, 291 (2023) 116407; <https://doi.org/10.1016/j.mseb.2023.116407>
- [8] A.U. Rehman, N. Amin, M.B. Tahir, M.A. un Nabi, N. Morley, M. Alzaid, M. Amami, M. Akhtar, M.I. Arshad, *Materials Chemistry and Physics*, 275 (2022) 125301; <https://doi.org/10.1016/j.matchemphys.2021.125301>
- [9] K.L. Routray, S. Saha, D. Behera, *Materials Science and Engineering: B*, 257 (2020) 114548; <https://doi.org/10.1016/j.mseb.2020.114548>
- [10] S. Saha, K.L. Routray, P. Hota, B. Dash, S. Yoshimura, S. Ratha, T.K. Nayak, *Journal of Molecular Structure*, 1302 (2024) 137409; <https://doi.org/10.1016/j.molstruc.2023.137409>
- [11] K. Sakthipandi, K. Venkatesan, R. Sivakumar, G. Rajkumar, B.G. Babu, S. Arunmetha, A. Hossain, M.S. Raghavan, V. Rajendran, *Journal of Alloys and Compounds*, 981 (2024) 173708; <https://doi.org/10.1016/j.jallcom.2024.173708>
- [12] M.U. Khalid, M. Ajaz-un-Nabi, M.I. Arshad, A.U. Rehman, K. Hussain, S. Arshad, Z.M. El-Bahy, M.E. El Sayed, N. Amin, *Ceramics International*, 50 (2024) 24025-24035; <https://doi.org/10.1016/j.ceramint.2024.04.134>
- [13] S. Arshad, M.I. Arshad, A.U. Rehman, N. Amin, M.J.M.S. Ajaz-un-Nabi, E. B, *Graphene nanoplatelets/Li-Mg-Sm spinel ferrite nanocomposites with improved dielectric and magnetic properties*, 299 (2024) 117019; <https://doi.org/10.1016/j.mseb.2023.117019>
- [14] R. Shu, Y. Wu, Z. Li, J. Zhang, Z. Wan, Y. Liu, M. Zheng, *Composites Science and Technology*, 184 (2019) 107839; <https://doi.org/10.1016/j.compscitech.2019.107839>
- [15] G. Shweta, L. Naik, R. Pujar, S. Mathad, *Materials Chemistry and Physics*, 257 (2021) 123825; <https://doi.org/10.1016/j.matchemphys.2020.123825>

- [16] K. Mehmood, A.U. Rehman, N. Amin, N. Morley, M.I. Arshad, *Journal of Alloys and Compounds*, 930 (2023) 167335; <https://doi.org/10.1016/j.jallcom.2022.167335>
- [17] G. Hussain, I. Ahmed, A.U. Rehman, M.U. Subhani, N. Morley, M. Akhtar, M.I. Arshad, H. Anwar, *Journal of Alloys and Compounds*, 919 (2022) 165743; <https://doi.org/10.1016/j.jallcom.2022.165743>
- [18] M.I.U. Haq, A.u. Rehman, M. Asghar, M.A.U. Nabi, N. Amin, S. Tahir, M.I. Arshad, *Journal of Superconductivity and Novel Magnetism*, 35 (2022) 719-732; <https://doi.org/10.1007/s10948-021-06124-1>
- [19] G. Abbas, A.U. Rehman, W. Gull, M. Afzaal, N. Amin, L. Ben Farhat, M. Amami, N.A. Morley, M. Akhtar, M.I. Arshad, *Journal of Sol-Gel Science and Technology*, 101 (2022) 428-442; <https://doi.org/10.1007/s10971-021-05713-9>
- [20] N. Amin, A. Razaq, A.U. Rehman, K. Hussain, M.A.U. Nabi, N. Morley, M. Amami, A. Bibi, M.I. Arshad, K. Mahmood, *Journal of Superconductivity and Novel Magnetism*, 34 (2021) 2945-2955; <https://doi.org/10.1007/s10948-021-06053-z>
- [21] A.M. Abu-Dief, M.S. Abdelbaky, D. Martínez-Blanco, Z. Amghouz, S. García-Granda, *Materials Chemistry and Physics*, 174 (2016) 164-171; <https://doi.org/10.1016/j.matchemphys.2016.02.065>
- [22] A. Abouhaswa, M. Badr, H. Abomostafa, *Inorganic Chemistry Communications*, (2024) 112647; <https://doi.org/10.1016/j.inoche.2024.112647>
- [23] M. Abdullah-Al-Mamun, M. Sarker, M. Hasan, M. Haque, F. Khan, M. Rahman, M. Khan, *Results in Physics*, 29 (2021) 104698; <https://doi.org/10.1016/j.rinp.2021.104698>